university of groningen / faculty of science and engineering / kapteyn astronomical institute

Rijksuniversiteit Groningen

Bachelor Thesis Astronomy

Searching for and analysing molecular lines in ALMA data of the protoplanetary disk around TW Hya

Author:
Susan de Vries

Supervisors:
Prof. Dr. I.E.E. Kamp
Dr. C. Rab

Second Examiner:
Dr. R. F. Shipman

July 11, 2019

Abstract

Context. With ALMA high spatial and spectral resolution observations of protoplanetary disks can be made. With such data the structure and chemical composition of these disks can be studied

Goals. The goal of this thesis is to analyse ALMA data of the protoplanetary disk TW Hya. The observation targeted CO^+ lines, but also showed indications for the detection of some other molecular lines. For this project these lines will be looked for and identified. The produced line cubes will be analysed and structures in the disk, such as gaps, holes and rings, identified.

Methods. The data processing software `CASA` was used to examine and work with the data, by e.g. producing moment maps and calculating line fluxes.

Results and conclusions. Four emission lines are found in the data, all caused by rotational transitions. The lines and their fluxes are: 0.331 $\pm$ 0.093 Jy km s^{-1} for DCN J $= 3-2$, 0.10 $\pm$ 0.16 Jy km s^{-1} for ^{13}CN $\mathbf{N} = 2-1$, 0.63 $\pm$ 0.22 Jy km s^{-1} for C^{18}O J $= 2-1$ and 2.28 $\pm$ 0.30 Jy km s^{-1} for ^{13}CO J $= 2-1$. For ^{13}CN $\mathbf{N} = 2-1$ this is a first detection, it can therefore only be compared to the previously observed more abundant ^{12}CN $\mathbf{N} = 2-1$. The ^{13}CN flux is significantly lower than the ^{12}CN flux, as expected. The fluxes of the other lines agree, within the error bars, with the literature. As no emission was found for the CO^+ lines only an upper limit can be set on the flux. These upper limits are approximately 0.046 Jy km s^{-1} for the CO^+ J $= 2-1$, $\mathbf{F} = \frac{3}{2} - \frac{1}{2}$ transition and 0.040 Jy km s^{-1} for the CO^+ J $= 2-1$, $\mathbf{F} = \frac{5}{2} - \frac{3}{2}$ transition.

The moment maps and radial flux profiles created can give an indication of the physical and chemical structure of the disk. The DCN J $= 3-2$ emission shows a ring shape, C^{18}O J $= 2-1$ and ^{13}CO J $= 2-1$ are centrally peaked. The ^{13}CN $\mathbf{N} = 2-1$ has a too low signal to noise ratio to determine a definite shape. The peak fluxes of ^{13}CN $\mathbf{N} = 2-1$, however, do coincide with the location of a previously found ring structure for ^{12}CN $\mathbf{N} = 2-1$. This suggests they have a similar ring structure. Radial flux profiles of the lines show that DCN J $= 3-2$ and ^{13}CN $\mathbf{N} = 2-1$ have their peak emission at a distance of 42 $\pm$ 15 AU from the centre of the disk. The C^{18}O J $= 2-1$ and ^{13}CO J $= 2-1$ radial flux profiles show a plateau in the emission between $\sim$ (30-65)$\pm$ 15 AU, this is consistent with the literature. Finally for C^{18}O J $= 2-1$ and ^{13}CO J $= 2-1$ radial temperature profiles are also made. They show a flat profile with temperatures around 16 K in the inner 60 AU, which then gradually decrease to $\sim$ 8 K at 100 AU. Compared to literature these values are lower. This may be explained by the fact that our data has a lower velocity resolution than the data from the literature.

Acknowledgements

First I would like to thank my supervisors Inga and Christian for guiding me through this project and being available to help me when needed. Their support and knowledge allowed me to truly grasp the important concepts in this project. I would like to thank Alex Taun for providing me with some `CASA` code.

Besides that I would also like to thank some of my fellow students; Janke, Ylse, Jasper, Sebastiaan, Lorraine and Marit for keeping me company, helping me with various problems and for sharing the ups and downs of working on a bachelor thesis.

Contents

1 Introduction

To understand how structures such as our own solar system have formed it is useful to observe similar systems during different stages of evolution. An example of such a system is a protoplanetary disk. It is the place where planets are being formed to eventually create a planetary system possibly comparable to our own.

As with most astronomical objects, we learn about protoplanetary disks via observations. We can learn about the disks chemistry and structure, which may have features such as holes, rings and gaps, by looking at its spectral line emission. To give an idea of the types of research possible with molecular emission lines some more specific examples will be given. From the location of certain molecules in the disk, for example, the effectivity of chemical reactions can be determined. Emission from more complex molecules can teach us about how the building blocks of life itself can exist in these regions of star and planet formation [Henning and Semenov, 2013]. Another example concerns temperatures. From line intensities radial temperature profiles of the disk can be derived. Locations of for example ice lines can also be found. These play an important role in the formation and location of planets in the disk, as the ice line is where planetesimals will form first [Drążkowska and Alibert, 2017]. Finally deuterated species in general are very interesting. They can for example be used to study the thermal history of pre-stellar environments [Salinas et al., 2017], or to learn about D/H ratios in systems other than our own.

In this introduction ideas and theory important for this thesis will be presented. This includes some information about protoplanetary disks, in particular TW Hya, as well as molecules and their emission lines. ALMA, the telescope with which the data was taken, will also be shortly introduced. After the introduction the methods with which the data was obtained and processed will be discussed in Sect. 3. The results obtained are presented in Sect. 4 and discussed in Sect. 5. A conclusion and future possibilities will be given in Sect. 6.

1.1 Protoplanetary disks

A protoplanetary disk is a circumstellar disk centred around a young star. The disk is composed of dense gas and dust and forms when the gas cloud surrounding a young star collapses. Due to conservation of angular momentum the collapsed cloud will become disk shaped and a protoplanetary disk is formed. In here small clumps of material will form as the dust sticks together cohesively. Once chunks of a certain size are formed gravity will start to play a role. In regions of over-density, gravity will start a process of oligarchic growth. The largest initial piece will grow fastest, and so planet(esimal)s form. [de Pater and Lissauer, 2015].

1.1.1 Disk structure

The physical and chemical structure of a protoplanetary disk around a young solar-like star can be seen in Fig.1 [Henning and Semenov, 2013]. A quite prominent feature is the flaring of the disk. The ratio of the disk's thickness to the distance from the centre increases with the distance. This means that the surface of the disk receives light directly from the star, as it is not blocked by other parts of the disk. This can also be seen in Fig. 1. The right side of this image displays the temperature of the disk. It shows that with radius the temperature of the midplane decreases quicker than that of the surface. The inner part of the disk has dust temperatures up to 1500 K, the gas can reach several 1000 K (e.g. [Woitke et al., 2009]). A temperature model made for TW Hya, more specifically, shows that at 100 AU temperatures in the midplane drop below 10 K, while at the surface they can still be above 40 K [Kamp et al., 2013]. Thus there is a temperature gradient in both the horizontal and vertical direction.

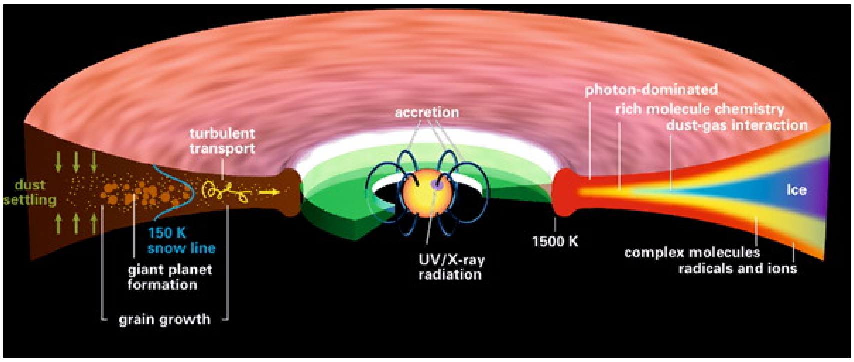

Fig. 1: Sketch of the structure of a protoplanetary disk surrounding a Sun-like star. Credit: [Henning and Semenov, 2013].

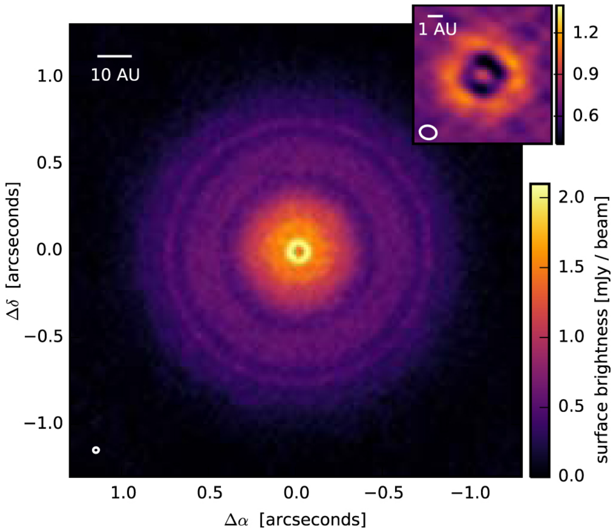

Fig. 2: A synthesized image of the 870 μm continuum emission for the disk surrounding TW Hya. Image taken by ALMA with a circular beam of 30 mas. The image in the upper right shows a 0.2 arcsec zoom taken with a 18 by 24 mas beam. Note: In this image the distance to the disk was taken as 54 pc. As the real distance is 60.086 pc [Gaia Collaboration, 2018] the bar in the upper left displays a size of roughly 11 AU. Credit: [Andrews et al., 2016]

.

1.1.2 TW Hya

The protoplanetary disk studied in this thesis is the TW Hya disk. This disk is well studied since it is relatively nearby, $d = 60.086$ pc [Gaia Collaboration, 2018], and has a nearly face on orientation with an inclination of $(7 \pm 1)^\circ$ [Qi et al., 2004]. An image of the TW Hya disk is seen in Fig. 2. The image, taken by ALMA, shows the 870 μm continuum emission with a circular beam of 30 mas [Andrews et al., 2016]. The image demonstrates that structure in this disk has been observed previously and that ALMA is capable of creating very high angular resolution images.

The star in the disk's centre is a so called T-Tauri star. These stars are characterised by being young ($\lesssim$10 Myr)[Appenzeller and Mundt, 1989], pre-main-sequence and of spectral type F-M [Henning and Semenov, 2013]. The disk is moving away from us with a systemic velocity of 2.84 km s^{-1} [Huang et al., 2018].

1.2 Molecules

1.2.1 Molecular lines

Atoms and molecules can absorb energy causing them to go into an excited state. If this excitation is followed by radiative de-excitation, the energy is released again in the form of light. The energy and frequency of light are related via:

$$E = h\nu \tag{1}$$

with h being the Planck constant. As molecules can only take on discrete energy levels, excitation and de-excitation are confined to specific frequencies. The light that is emitted by de-excitation therefore has a unique frequency. Hence, by observing a source and looking at which frequency emission occurs atomic and molecular species can be identified.

Several types of excitation are possible, in descending energy these are: electronic, vibrational and rotational excitation. For electronic excitation an electron is brought to a higher level and de-excitation occurs when it falls back to a lower level. This can occur in one step, from the excited level back to the ground level, or in multiple steps. Electronic transitions emit in the UV/visible range of the electromagnetic spectrum. Vibrational excitation occurs at somewhat lower energies. Here atoms in the molecule vibrate with respect to each other. Vibrational transitions emit in the infrared part of the electromagnetic spectrum. Finally rotational excitation, this type of excitation requires the smallest amount of energy. In this case the entire molecule is rotating, it emits in the microwave/radio part of the electromagnetic spectrum. This is the most relevant case for this thesis as the observation was done at mm wavelengths. At such low energies only rotational lines can be detected. This means that all the molecular lines later presented in this thesis are rotational lines.

1.2.2 Molecular spectroscopy

The proton number of an atom is what determines the species, the neutron number however can differ. Versions of atoms with the same proton number but a different neutron number are called isotopes. Molecules of the same atomic composition containing different isotopes are called isotopologues. Isotopes are denoted by writing the neutron number in front of the atom it refers to. Take as an example CO, one of its isotopologues is $C^{18}O$, here no number is written in front of the C meaning it is the most abundant isotope (^{12}C).

As mentioned, molecular species can be identified by looking at the frequency of the emitted light. As each isotopologue is slightly different, their excitation energies differ, meaning these can also be identified by looking at molecular spectra.

Atomic and molecular transitions can be specified with the help of quantum numbers. For electronic, vibrational and rotational transitions we have the corresponding electronic, vibrational and rotational quantum number. These are usually denoted by the letters n, v and J respectively. For most of the lines found later in this thesis these numbers are enough. One of the molecules, however, has a more complicated coupling scheme and requires the introduction of more quantum numbers. The molecule in question is ^{13}CN, see Table 1. Its coupling scheme has been described previously [Savage et al., 2002]. For ^{13}CN the line splitting can be described best by Hund's case b. Hund's cases are simplified or idealised ways of describing coupling processes in diatomic molecules. In this case the coupling of the electronic orbital and electronic spin angular momentum, denoted by **L** and **S** respectively, is very weak or even vanishes [Brown and Carrington, 2003]. The spin-orbit coupling vanishes when Λ, the projection of the orbital angular momentum on the inter-nuclear axis, is zero. First, the coupling for a molecule in which only one of the atoms has nuclear spin angular momentum, **I**, will be described. This way it is easier to show why ^{13}CN is a special case. As there is no spin-orbit coupling, the electronic spin angular momentum, $\mathbf{S}$, will instead couple to the molecular frame rotation, $\mathbf{N}$. Together they form a total angular momentum $\mathbf{J}$, $\mathbf{N}+\mathbf{S}=\mathbf{J}$. $\mathbf{J}$ is also called the fine-structure. If there is one nuclear spin angular momentum, $\mathbf{I}$, it would then couple to $\mathbf{J}$ to form $\mathbf{F}$: $\mathbf{I}+\mathbf{J}=\mathbf{F}$. This $\mathbf{F}$ is another total angular momentum which denotes the hyperfine levels. In the case of ^{13}CN both the carbon and the nitrogen carry a nuclear spin, making the coupling even more complicated. Here, the first coupling is between $\mathbf{S}$ and the nuclear spin of ^{13}C, denoted by $\mathbf{I}_1$. This gives: $\mathbf{S}+\mathbf{I}_1=\mathbf{F}_1$. The created first angular momentum will then couple to the molecular frame rotation, $\mathbf{N}$, to form the second angular momentum: $\mathbf{N}+\mathbf{F}_1=\mathbf{F}_2$. Finally, the total angular momentum of ^{13}CN is formed when the second angular momentum couples with the nitrogen nuclear spin, denoted by $\mathbf{I}_2$. We thus have $\mathbf{F}=\mathbf{F}_2+\mathbf{I}_2$.

With the quantum numbers presented all line transitions in this thesis can be identified as shown in Table 1. The frequencies given in this table will be rounded to two decimals in the rest of this thesis for readability. For more information about the lines see Sect. 4.

Species	Rest freq.(GHz)	Quantum numbers	$E_{\text{upper level}}$ (K)
DCN	217.23853	$v=0$, $J=3-2$	20.8511
^{13}CN	217.46715	$\mathbf{N}=2-1$, $\mathbf{J}=\frac{5}{2}-\frac{3}{2}$, $\mathbf{F}_1=3-2$, $\mathbf{F}=4-3$	15.6842
	217.46715	$\mathbf{N}=2-1$, $\mathbf{J}=\frac{5}{2}-\frac{3}{2}$, $\mathbf{F}_1=3-2$, $\mathbf{F}=3-2$	15.6849
	217.46915	$\mathbf{N}=2-1$, $\mathbf{J}=\frac{5}{2}-\frac{3}{2}$, $\mathbf{F}_1=3-2$, $\mathbf{F}=2-1$	15.6856
$C^{18}O$	219.56036	$J=2-1$	15.8059
^{13}CO	220.39868	$J=2-1$	15.8663

Table 1: An overview of the lines present in the data.

1.2.3 Molecules in the disk

Different molecules can trace different parts of the disk. Molecular emission that becomes optically thick quickly will only trace the disk down to a certain depth. Photons emitted from deeper layers will be absorbed by the molecule itself before reaching the surface of the disk. The light originating from these deeper layers will thus not be observed. Molecular lines that are optically thinner can trace way further into the disk. As mentioned before protoplanetary disks have a vertical and horizontal temperature gradient. Therefore, optically thick emission generally traces the warmer surface layers of the disk, while optically thinner emission traces the cooler parts closer to the midplane.

Other factors also play a role in whether a molecule traces deep into the disk or not. Some molecules will only exist in a certain part of the disk due to, for example, formation pathways only working at certain temperatures. Emission from such a molecule will then trace the depth at which the molecule resides.

1.3 ALMA

The data used for this project was taken by ALMA, the Atacama Large Millimeter/submillimeter Array. It is situated in the Atacama desert in Chile, which due to its altitude and dryness is an ideal location for a telescope. ALMA consists of 66 antennas with a maximum baseline of 16 km [ALMA (ESO/NAOJ/NRAO), 2019]. The antennas work together as one using interferometry. Interferometry is a technique based on the interference of light waves. When two waves are combined they interfere, resulting in a wave with either a larger or smaller amplitude than the initial ones. An interferometer, such as ALMA, is a setup in which 2 or more telescopes are combined and their signals correlated.

For a single telescope its angular resolution is given by: $\theta = \frac{\lambda}{D}$, where λ is the observing wavelength and D the diameter of the telescope dish. For multiple telescopes this formula changes to:

$$\theta = \frac{\lambda}{b}, \tag{2}$$

where b is the baseline between the telescopes. By taking larger distances between the telescopes we can thus get very high angular resolutions.

ALMA observes in the millimeter and submillimeter wavelength range. These are waves in between the far infrared and radio, which are on the lower energy side of the electromagnetic (EM) spectrum. As of this moment, 8 out of the 10 planned ALMA bands are working. For ALMA the frequency range is approximately 84 to 950 GHz, and the highest angular resolution that can be obtained is around 10 mas [ALMA (ESO/NAOJ/NRAO), 2019]. The data used in this thesis was taken in band 6, spanning a frequency range of 211-275 GHz [ALMA (ESO/NAOJ/NRAO), 2019]. Examples of lines previously found in protoplanetary disks that could show up in this band include transitions of: HCN and DCN J $= 3-2$, SiO J $= 6-5$, J $= 5-4$, HCO^+ and DCO^+ J $= 3-2$, CO J $= 2-1$ and various $\mathbf{N} = 2-1$ transitions of the cyanide radical. Note that to keep the above list comprehensible only the species were mentioned, not the various isotopologues.

The combination of the high resolution and frequency range makes ALMA the ideal telescope to look for molecular emission in protoplanetary disks.

2 Data

The ALMA data used in this project was originally taken for Christian Rab who wanted to study the possible disk wind of TW Hya using CO^+ emission lines. Due to the high-energy radiation emitted by the star (X-rays, FUV), the upper layers of protoplanetary disks can become hot enough for gas particles to reach escape velocity. This is called a photo-evaporative, or thermal, wind. The vertical layer of the disk where this condition is still full-filled is called the flow-base. Photo-evaporative winds might play an important role in the dispersal of disks [Ercolano and Pascucci, 2017].

Unfortunately CO^+ was not detected and the data-set was not yet inspected further. In this thesis I look for and investigate other emission lines present in the data-set.

The title of the observing proposal is 'Searching for the flow base of the disk wind in TW Hya' with ID 2016.1.01375.S. The data was taken with the 12m array (40 antennas) in receiver band 6 and configuration C40-4. The requested angular resolution and Largest Angular Scale (LAS) were 0.40 and 3.0 arcsec respectively. The beam has an elliptical shape and it varies slightly with spectral window. The approximate minor and major axis are given in Table 2. Since the disk is at a distance of 60.086 pc [Gaia Collaboration, 2018], a beam size of ~ 0.47 arcsec translates to a size of roughly 28 AU in the disk. Comparing this to the size of the disk, Fig. 3, we see that the disk is resolved. The data is divided over five spectral windows (SPW), which cover the frequency ranges shown in Table 2. Every spectral window is composed of a number of channels which are also shown in Table 2. Two adjacent channels will differ in their velocity. This spacing between them is called the velocity, or spectral, resolution.

The CO^+ lines targeted are the CO^+ $J = 2-1$, $\mathbf{F} = \frac{5}{2} - \frac{3}{2}$ transition with a rest frequency of approximately 236.06 GHz and the CO^+ $J = 2-1$, $\mathbf{F} = \frac{3}{2} - \frac{1}{2}$ transition with a rest frequency of approximately 235.79 GHz. Here J is the rotational quantum number and $\mathbf{F}$ denotes the hyperfine structure. Looking at the table we see that the CO^+ $J = 2-1$, $\mathbf{F} = \frac{5}{2} - \frac{3}{2}$ transition should be seen in spectral window five, the CO^+ $J = 2-1$, $\mathbf{F} = \frac{3}{2} - \frac{1}{2}$ transition in spectral window four.

The data I use in this thesis is a standard pipeline product provided by ALMA. The pipeline product was used directly as the data quality was slightly better than requested, an rms of roughly 2.5 mJy beam^{-1} channel^{-1} instead of 3 mJy beam^{-1} channel^{-1}. Upon retrieval it had been calibrated, flagged, cleaned and corrected for the primary beam.

SPW	Frequency (GHz)	Number of channels	Beam size (arcsec)	Vel. res. (km/s)
1	216.634 - 217.571	3807	0.488 × 0.475	0.34
2	219.499 - 219.616	500	0.474 × 0.466	0.32
3	220.337 - 220.454	498	0.471 × 0.464	0.32
4	235.669 - 235.904	931	0.443 × 0.435	0.32
5	235.942 - 236.177	930	0.443 × 0.435	0.32

Table 2: An overview of the spectral windows the data was split up in.

3 Methods

3.1 Identification of emission lines

For this thesis the data was mostly processed using `CASA` [McMullin et al., 2007]. First the images were inspected using `imview`, and clear emission showed up in the first three spectral windows. With the `Spectral Profile Tool` spectral profiles were made of all five spectral windows. The `Line Overlays` tool, which uses the data from Splatalogue [NRAO, 2012], allowed for the first identification of the emission lines. Using the systemic velocity of TW Hya previously mentioned, four lines were found in the first three spectral windows. The first spectral window contains lines of DCN J $= 3-2$ and ^{13}CN $\mathbf{N} = 2-1$. In the second and third spectral window a C^{18}O J $= 2-1$ and ^{13}CO J $= 2-1$ line are present, respectively.

3.2 Creating line cubes

Now that the lines had been found the emission could be isolated. In other words, the channels in which emission was present could be cut out of the large data set. This was done with the `CASA` task `imsubimage`. The cropped data sets are called line cubes. For the first three spectral windows this was done by cutting out the channels that contained the emission. In the fourth and fifth spectral window no clear emission was present. Here the channels corresponding to the frequencies the emission would be at, if it were present, were cut out. As the ^{13}CN $\mathbf{N} = 2-1$ line is composed of transitions very closely spaced together, see Table 1 and Fig. 4b, the processes undertaken for it differed slightly from those for the other lines. When things were done differently for ^{13}CN this will be mentioned.

When tasks such as `imsubimage` are performed, the output files `CASA` gives are 'CASA images'. When needed, for example to plot them in a notebook, they were converted into the more common fits file format, with `exportfits`.

3.3 Producing moment maps

Cutting down the data makes it easier to handle and allows for the creation of moment maps. With moment maps one can reduce a 3D image, the line cube, to a 2D image. To create moment 0, and 8 maps `immoments` was used. Moment 0 maps are created by integrating the line cube over the velocity (frequency) axis. For a moment 8 map, the peak flux in each pixel present in any of the channels of the line cube is picked. With all these maxima a new image is created.

When the moments are calculated, regions and masks can be applied. Here a region refers to an area of a certain size encompassing the emission, while a mask refers to a lower bound set on the pixel values. Both the region and mask were determined using `imview`. A first estimate of the region to use was made using the C^{18}O J $= 2-1$ and ^{13}CO J $= 2-1$ lines, since they both clearly show the centre and extent of the disk. Later on it was noted that this region did not fit every line equally well. New regions were determined for every line by eye. Some were made larger, as the emission seem ed to extend quite far, while others were made smaller, as no emission seemed to come from the outer parts of the image. To determine the mask, a box was drawn in an area in which no emission was expected. `imview` then gives information, such as the rms, about the selected part of the image. This was used to get a maximum and minimum value of the rms from the channels surrounding the emission. The average of these two values was taken as the mask value.

As the signal to noise ratio was very poor for the ^{13}CN $\mathbf{N} = 2-1$ line the decision was made to not use a mask for this line. A mask removed too much of the image, creating a very splotchy look, while not improving the visibility of the emission. Since the fourth and fifth spectral window showed no emission, a mask was not used for them either. The region was set to the same area as it was initially for the other spectral windows. For these spectral windows only a moment 0 map was created as the other moments would not give any extra insight.

The moment maps, especially the moment 0 map, are a great visual aid and contain useful information about the data. Distances in the image can be measured with a ruler in `imview`. The task `imstat` can be used for all kinds of `CASA` images, while `specflux` only works for line cubes. Both of these tasks give their output in an inconvenient format. `imstat` displays it in the `CASA` terminal, while `specflux` gives its output in the `CASA` logbook. Therefore a Python script was written. It runs the tasks for the specified images and puts the output in a `txt` file. This format was chosen as it can be easily opened with Python, allowing the data to be plotted.

3.4 Obtaining line fluxes and spectral profiles

Using the `imstat` task on the moment 0 map, the line fluxes are found. These values could then be compared to the literature values previously found for TW Hya. The values and the literature comparisons can be found in Sect. 4.3. Errors in the fluxes were determined from the spectral profiles of the lines. These are explained later in this section.

From the `specflux` task spectral profiles were made. These are plots showing flux vs velocity, which in our case have the units of Jy and km s^{-1}, respectively. The spectral profiles provide insight in the width and shape of the line. They can be seen in Fig. 4. The profiles shown are without a mask and are wider than the ones used for the creation of the moment maps. This was done to show the noise surrounding the line. Each channel in the line cube results in one data point for the spectral profile. By creating a line cube with more or less channels, and making the corresponding spectral profiles, we can thus check if the initial size chosen for the line cubes (used for the moment maps) includes all emission. Where needed the line cubes were remade with more or less channels. In the spectral profiles, Fig. 4, the channels with which the moment maps were made are indicated by vertical lines. These widths were chosen such that only the line emission was included.

Due to separation of the hyperfine structure for the ^{13}CN $\mathbf{N} = 2-1$ emission, Fig. 4b, there are multiple ways in which the line cube can be cut. First it was decided to cut as closely as possible around the emission to have the least amount of noise. Another possibility is to cut the peaks out separately. They can then be overlaid and a moment map can be created. This was done in the hope that by excluding the few points in-between the two peaks the signal to noise ratio would improve. Unfortunately the image quality did not improve significantly by doing this. It was thus chosen to make a single cut around the two peaks.

The errors in the line fluxes were determined from the standard deviation of the noise present in the spectral profiles, and used to get 3σ values. These were then multiplied by the width of the profile in km s^{-1} to get the total error in the line flux. The spectral profiles used to determine this noise were made without a mask and were made wider than the ones shown in Fig. 4. This was done to get a more accurate estimate of the noise.

Note that the data was originally taken to observe CO^+ and CO lines. Therefore only the spectral windows in which CO emission was present were aligned properly, meaning that the systemic velocity of the disk coincides with the rest frequency of the line. Since the first spectral window is the only one containing no CO emission, it only had to be corrected here. This was done by putting the rest frequencies of the lines, DCN J $= 3-2$ and ^{13}CN $\mathbf{N} = 2-1$, in the image header of the line cubes. They were put in using `imhead` with: hdkey = 'RESTFREQ', hdvalue = the rest frequency of the corresponding line. For ^{13}CN $\mathbf{N} = 2-1$ the frequency of the strongest of the two peaks was set as the rest frequency. After this the spectral profiles were properly centred at the systemic velocity.

3.5 Creating radial flux profiles

From the moment 0 map one can also make azimuthally averaged radial flux profiles. These are profiles showing the flux as a function of distance from the centre of the disk. For this a Python script made by Alex Taun was adapted. In the code, annuli are created which all have the same width in arcsec. The flux in this annulus is calculated with `imstat` and divided by the area of the annulus. The outer radius of the previous annulus is then set as the inner radius of the next one and this process is repeated until the end of the image is reached. The thickness of the annulus, or the difference between the inner and outer radius, was set to 0.2 arcsec. This value was chosen as it generated an acceptable amount of data points, while not being too small compared to the beamsize of roughly 0.5 arcsec. As each annulus has a certain thickness, the radius corresponding to the calculated flux was set as the average of the inner and outer radius. This does mean that the radial flux profiles will not start at zero, but instead start at the average of the first inner and outer radius, which is at 0.1 arcsec. This corresponds to a size of roughly 6 AU in the disk. Errors in the radial flux profiles were determined by dividing the rms noise in the moment 0 images by the square root of the number of independent beams in each annulus [Isella et al., 2016]. As the rms needs to be determined from a region of no emission, the moment 0 maps used for this were not masked, nor was a region applied to them. The radial flux profiles can be seen in Fig. 6. Besides the line images, the data I was provided with also contained continuum images. From these a radial flux profile was made as well with the method previously described. The radial flux profiles containing both the line and continuum flux are show in Fig. 7.

As radial flux profiles of $C^{18}O$ and ^{13}CO have been made previously, [Schwarz et al., 2016], these could be used to compare my result with. To do this a digitized version of Schwarz's image was made with an online tool, WebPlotDigitizer [Rohatgi, 2019]. To compare the shapes of the profiles with those in this thesis, some modifications had to be made. First of all in Schwarz's paper the distance to the disk is set at 54 AU. The new GAIA release found a larger distance, 60.086 AU [Gaia Collaboration, 2018]. The radii found by Schwarz need to be corrected for this. Besides that, Schwarz's data is normalised to 1 at the centre of the disk. As my radial flux profiles start at a small distance from the centre, this had to be corrected for. Using an interpolation routine in Python, the flux of Schwarz's profile at ∼6 AU, was found. This value was then used to re-normalise Schwarz's data such that the flux was 1 at my starting point. The final combined data can be seen in Fig. 8.

3.6 Radial temperature profiles for $C^{18}O$ $J = 2-1$ and ^{13}CO $J = 2-1$

For $C^{18}O$ $J = 2-1$ and ^{13}CO $J = 2-1$ another type of radial profile can also be made. These are radial temperature profiles, which have been made previously for other rotational transitions of $C^{18}O$ and ^{13}CO [Schwarz et al., 2016]. The first step in creating this temperature profile is solving for Eq.(3). The equation relates the brightness temperature T_B, excitation temperature T_{ex} and optical depth τ [Schwarz et al., 2016].

$$\frac{T_B(^{13}\mathrm{CO})}{T_B(\mathrm{C}^{18}\mathrm{O})} = \frac{T_{ex,^{13}\mathrm{CO}}(1-\mathrm{e}^{-\tau_{^{13}\mathrm{CO}}})}{T_{ex,\mathrm{C}^{18}\mathrm{O}}(1-\mathrm{e}^{-\tau_{\mathrm{C}^{18}\mathrm{O}}})} \tag{3}$$

Now the ratio of brightness temperatures on the left hand side of Eq.(3) can be expressed as a ratio of intensities via the Rayleigh Jeans expression. This is an approximation of Planck's law, which describes the brightness of a black body at a temperature T. The Rayleigh Jeans approximation holds in the long wavelength regime of the electromagnetic spectrum and is given by:

$$I_\nu = \frac{2kT_B\nu^2}{c^2}. \tag{4}$$

Now as the speed of light, c, and the Boltzmann constant, k, are constants they cancel when two intensities are divided. The frequencies and excitation temperatures of the isotopologues are very close, see Table 1. For $C^{18}O$ J $= 2 - 1$ we have: $\nu \approx 219.56$ GHz, $T_{ex} = 15.8059$ K, while for ^{13}CO J $= 2-1$ the frequency and temperature are: $\nu \approx 220.40$ GHz, $T_{ex} = 15.8663$ K. Assuming LTE, Eq.(3) then simplifies into:

$$\frac{I_{\nu,^{13}\mathrm{CO}}}{I_{\nu,\mathrm{C}^{18}\mathrm{O}}} = \frac{(1 - \mathrm{e}^{-\tau_{^{13}\mathrm{CO}}})}{(1 - \mathrm{e}^{-\tau_{\mathrm{C}^{18}\mathrm{O}}})}. \tag{5}$$

For the ratio on the left hand side of Eq.(5) we will use the masked moment 8 maps. Moment 8 maps are used as they represent the peak emission in each channel, which is a better measure of the temperature [Schwarz et al., 2016], [Weaver et al., 2018].

This leaves us with two unknowns, both optical depths, and just one equation. Luckily this can be solved for by assuming that the ratio of their optical depths, $\tau_{^{13}\mathrm{CO}}/\tau_{\mathrm{C}^{18}\mathrm{O}}$, is equal to the ratio of their abundances, $^{13}CO/C^{18}O$, which is roughly 8 [Schwarz et al., 2016]. Since we are now able to express one optical depth in terms of the other, $\tau_{^{13}\mathrm{CO}} = 8\tau_{\mathrm{C}^{18}\mathrm{O}}$, Eq.(5) can be solved numerically for $\tau_{^{13}\mathrm{CO}}$ and $\tau_{\mathrm{C}^{18}\mathrm{O}}$. Note that this can only be done when one of the lines is optically thick, which we assume the ^{13}CO J $= 2 - 1$ to be [Schwarz et al., 2016]. For $\tau_{^{13}\mathrm{CO}}$ and $\tau_{\mathrm{C}^{18}\mathrm{O}}$ a radial optical depth profile was made to check the assumption of ^{13}CO J $= 2 - 1$ being optically thick. This profile is shown in Fig. 9, how it was created will be explained later in this section.

The second equation that we need to determine the temperature profile, links the intensity, or brightness temperature, to the kinetic gas temperature T_K,

$$T_B = \frac{h\nu(1 - e^{-\tau_\nu})}{k\,\exp(h\nu/kT_K - 1)}. \tag{6}$$

Eq.(6) only holds assuming that the emission fills the beam, which is reasonable for resolved emission, and that we are in LTE [Schwarz et al., 2016]. The fluxes of our moment 8 maps can be converted to brightness temperatures in K, also considering the beamsize. Eq.(6) can be rewritten in the following way:

$$T_K = \frac{h\nu}{k}\left(\ln\left(\frac{h\nu}{kT_B}(1 - \mathrm{e}^{-\tau_\nu}) + 1\right)\right)^{-1}. \tag{7}$$

As T_K can now be solved for both $C^{18}O$ and ^{13}CO, an image can be created of the kinetic temperature in the disk. To create a radial temperature profile, the values for τ and T_B were first azimuthally averaged over a set of concentric rings in Python. A list of radii with a fixed stepsize of a third of the beamsize was created. This stepsize was chosen as it generated enough data points without being too small compared to the beamsize. For each pixel in the τ and T_B images the distance to the centre was calculated from its location. When pixels were less than one stepsize away from a set radius, their values were summed and averaged. Thus for each radius a corresponding average value of τ or T_B was determined. Finally the kinetic temperature was calculated with these averaged values of τ and T_B to create the radial temperature profile.

The variables with which T_K are determined are the brightness temperature, T_B, and the optical depth, τ. As they are related, see Eq.(7), their errors are related as well. To get an estimate of the error the following steps were taken. First a ratio image was made from moment 8 maps made without a mask or region. As the moment 8 maps are not masked they may contain pixel values close to zero, meaning that the ratio image might contain some extreme values. From the unmasked ratio image the standard deviation was measured in a region of no emission. As the standard deviation varied with the location in the image, it was determined 10 times in different parts of the image, and the average of this was taken as the 1σ value. The image was not modified in any way to account for the extreme values and thus the 1σ value is a conservative error. The optical depth was calculated twice. Once with this 1σ value added to the ratio, and once with this 1σ value subtracted from the ratio. The error this caused in τ was then propagated into T_K. T_K is calculated with Eq.(7), for the error in T_K only the error in τ was considered, not the error in T_B. The reason for this is that the uncertainty of T_B has been accounted for, in a way, in the τ derivation. Hence, to not overestimate the error, only the conservative error in τ was used. The resulting profile including the errors is compared to Schwarz's results in Fig. 10.

3.7 Determining flux upper limits for non-detected lines

For the fourth and fifth spectral window no spectral or radial profiles were made, as no line emission was found. However an upper limit on the CO^+ flux in the disk can be determined. The emission from ^{13}CO J $= 2 - 1$ is very extended. It can thus be assumed that if CO^+ were present in the disk it would emit at scales smaller than those of ^{13}CO J $= 2 - 1$. For ^{13}CO J $= 2 - 1$ the moment maps, Fig. 3g and Fig. 3h, show that most emission is emitted at radii $\lesssim 1$ arcsec. Therefore for CO^+ an image was created with a radius of 1 arcsec, as no emission is expected outside this scale. All pixels in this image were set at the rms value of the original moment 0 image. The flux of this image was then calculated with `imstat` as described previously. This was done for both spectral windows, the results can be found in Sect. 4.6.

4 Results

4.1 The molecules

As mentioned in the introduction four lines were found in the data. These are the DCN J $= 3-2$, ^{13}CN $\mathbf{N} = 2-1$, C^{18}O J $= 2-1$ and ^{13}CO J $= 2-1$ lines. In this section more information will be given on them.

In spectral window one the clearest line is DCN, or deuterium cyanide. The rest frequency of the line is at approximately 217.24 GHz. The transition occurs in the ground vibrational state, v $= 0$, and goes from rotational level 3 to 2, J $= 3-2$. The energy of the upper level is 20.8511 K. The other lines in this window are caused by a cyanide radical, ^{13}CN. These lines are actually caused by three transitions, two of which occur at the exact same frequency. They all have $\mathbf{N} = 2-1$, J $= \frac{5}{2} - \frac{3}{2}$ and $\mathbf{F}_1 = 3-2$. For the explanation of the hyperfine structure see Sect. 1.2.2. The transitions differ in the hyperfine transition. First $\mathbf{F} = 4-3$ and $\mathbf{F} = 3-2$, they both have a rest frequency of 217.46715 GHz. The other transition is $\mathbf{F} = 2-1$ with a rest frequency of 217.46915 GHz. The energy of the upper levels are 15.6824 K, 15.6894 K and 15.6856 K, respectively. In spectral window two, the only line present is due to C^{18}O, a carbon monoxide isotopologue. The rest frequency is at approximately 219.56 GHz, the transition is rotational from level 2-1, J $= 2-1$. The energy of the upper level is 15.8059 K. The line in spectral window three is also caused by a CO isotopologue, ^{13}CO. Here the rest frequency is at approximately 220.40 GHz and the transition is from rotational level 2 to 1, J $= 2-1$. The energy of the upper level is 15.8663 K. The information given is summarised in Table 1.

4.2 Moment maps

The moment maps created from the line cubes are shown in Fig. 3. The circle in the lower left corner of these images is a representation of the beam size, the FWHM of the beam. For ^{13}CN $\mathbf{N} = 2-1$ an extra circle is plotted. This circle represents a 0.9 arcsec ring that was previously found for a ^{12}CN $\mathbf{N} = 2-1$ transition in the TW Hya disk [Cazzoletti et al., 2018].

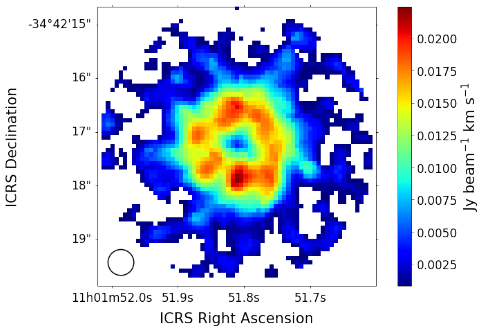

(a) Moment 0 map, DCN J = 3 − 2.

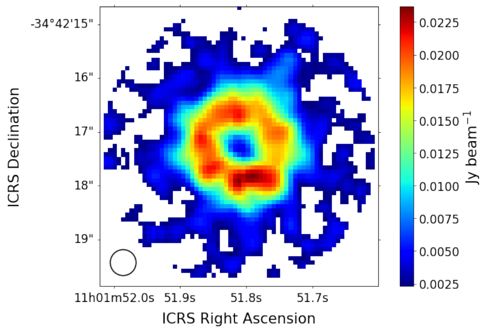

(b) Moment 8 map, DCN J = 3 − 2.

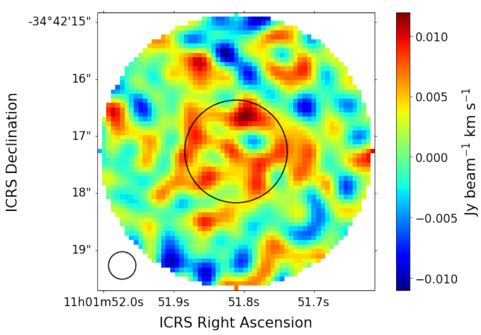

(c) Moment 0 map, ^{13}CN **N** = 2 − 1.

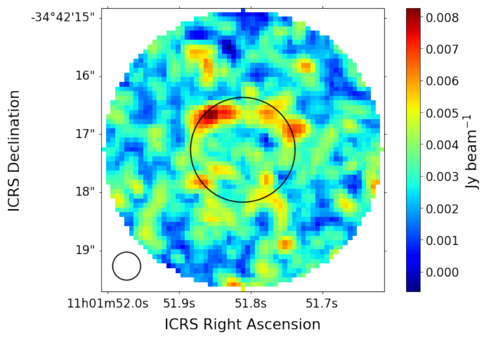

(d) Moment 8 map, ^{13}CN **N** = 2 − 1.

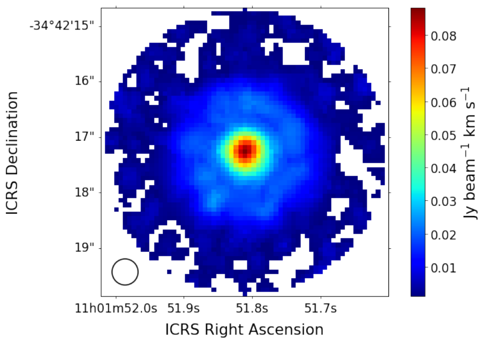

(e) Moment 0 map, C^{18}O J = 2 − 1.

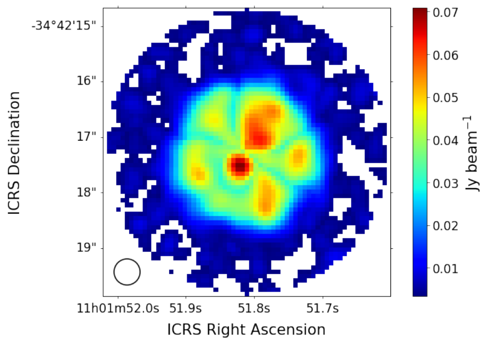

(f) Moment 8 map, C^{18}O J = 2 − 1.

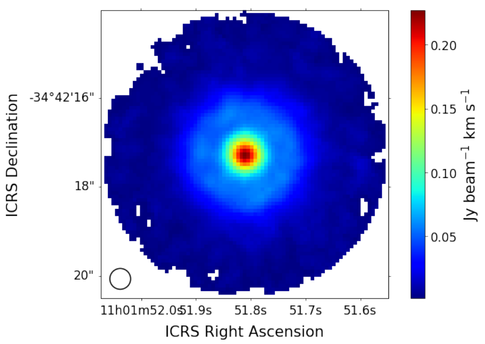

(g) Moment 0 map, ^{13}CO J = 2 − 1.

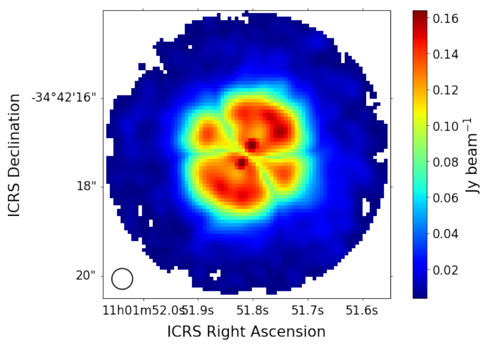

(h) Moment 8 map, ^{13}CO J = 2 − 1.

Fig. 3: The moment 0 and 8 maps for all lines in the first three spectral windows. The circle in the lower left represents the beamsize. The circle in ^{13}CN **N** = 2 − 1 indicates the location of the ^{12}CN **N** = 2 − 1 ring reported in [Cazzoletti et al., 2018].

Fig. 3a and 3b show the moment 0 and 8 map for DCN J $= 3-2$. From these images there appears to be a lack of emission in the centre of the disk, the size will be discussed at the end of Sect. 4.4. The ^{13}CN $\mathbf{N} = 2-1$ moment maps (Fig. 3c and 3d) look noisy. Especially in the moment 0 map it is hard to distinguish any structure at all. The moment 8 map shows some clear emission peaks which coincide with the ring structure previously found [Cazzoletti et al., 2018]. The ring has a radius of 0.9 arcsec, which corresponds to a distance of roughly 54 AU in the disk. For C^{18}O J $= 2-1$ and ^{13}CO J $= 2-1$ the emission is centrally peaked, with the latter being more extended. For C^{18}O J $= 2-1$ emission is visible up to around 1.5 arcsec from the centre, while for ^{13}CO J $= 2-1$ the maximal extend is closer to 2 arcsec.

The patterns visible in the moment 8 maps of the CO isotopologues are most likely due to the observational setup. This will be discussed in more detail in Sect. 5.3.

4.3 Line fluxes and spectral profiles

The spectral profiles of the lines are shown in Fig. 4. As there are multiple data points sampling the line profile it is spectrally resolved. For ^{13}CN $\mathbf{N} = 2-1$ two peaks are visible, this is caused by the separation of the hyperfine structure. The spectral profiles formed by a single transition have a single peak. The reason for this is that our disk is nearly face on, with an inclination of $(7 \pm 1)^\circ$ [Qi et al., 2004]. The line fluxes determined from the moment 0 map are given in Table 3. As a reminder the rounded frequencies are also given.

Line	Rest frequency (GHz)	Flux (Jy km s^{-1}), 3σ errors
DCN J $= 3-2$	217.24	0.331 $\pm$ 0.093
^{13}CN $\mathbf{N} = 2-1$	217.47	0.10 $\pm$ 0.16
C^{18}O J $= 2-1$	219.56	0.63$\pm$ 0.22
^{13}CO J $= 2-1$	220.40	2.28 $\pm$ 0.30

Table 3: The fluxes and errors found from the moment 0 map.

4.3.1 Comparison of fluxes to the literature

No lines fluxes could be found for DCN J $= 3-2$ and ^{13}CN $\mathbf{N} = 2-1$. For DCN J $= 3-2$ a spectral profile was found in the literature instead, Fig. 5a. For CN a moment 0 map of the main isotopologue ^{12}CN $\mathbf{N} = 2-1$, Fig. 5b, was found. The only comparison that can thus be done is to check that the ^{13}CN $\mathbf{N} = 2-1$ flux found is lower than in the literature as our isotopologue is rarer.

For DCN J $= 3-2$ the spectral profile peaks at approximately 0.25 $\pm$ 0.03 Jy, see Fig. 4a. The error is the original 3σ value, which has not been multiplied by the width of the profile. The one from the literature peaks at 0.31 Jy. This detection is not resolved however, and the error in this value is 0.1 Jy [Qi et al., 2008]. The fluxes thus overlap within the 3σ errors given.

The ^{13}CN $\mathbf{N} = 2-1$ moment map peaks at approximately 0.01 $\pm$ 0.02 Jy beam^{-1} km s^{-1}. The error given is a 3σ error determined from its moment map. The ^{12}CN $\mathbf{N} = 2-1$ from the literature peaks at a line flux of 0.6 Jy beam^{-1} km s^{-1}. These values cannot be compared directly however as there is still the unit of beam in both of them, and these are not equal. My beam size is approximately 0.475 by 0.488 arcsec, theirs 0.50 by 0.42 arcsec [Teague et al., 2016]. To compare them their line fluxes will be multiplied by their beam size, and then divided by my beam size. This results in a line flux of 0.54 Jy beam^{-1} km s^{-1}. The flux obtained is well below this one, roughly 50 times smaller. This is lower than the canonical ^{12}C/^{13}C isotope ratio of 69 [Visser et al., 2018]. This will be discussed in more detal in Sect. 5.2.

For C^{18}O J $= 2-1$ the derived line flux is 0.63 ± 0.22 Jy km s^{-1}. A literature value of $(6.0 \pm 1.3) \cdot 10^{-21}$ W m^{-2} (0.82 ± 0.18 Jy km s^{-1}) was found [Favre et al., 2013]. These values overlap also within the errors given. For the other CO line, ^{13}CO, the derived line flux is 2.28 ± 0.30 Jy km s^{-1}. For this line the literature value of $(20.0 \pm 1.3) \cdot 10^{-21}$ W m^{-2} (2.72 ± 0.18 Jy km s^{-1}) was found [Favre et al., 2013]. The values are consistent, within the error given, with our results.

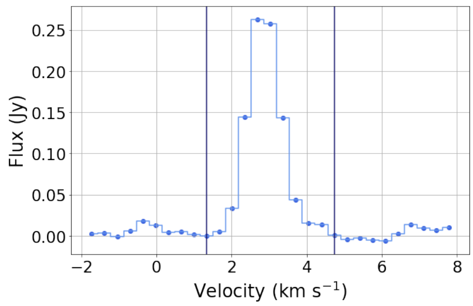

(a) Spectral profile DCN J $= 3-2$.

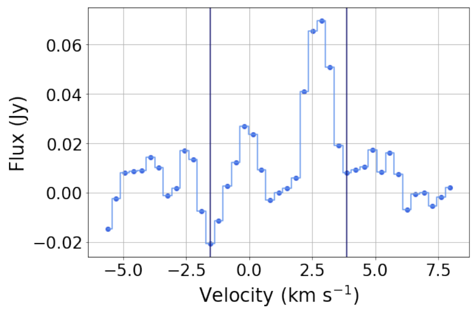

(b) Spectral profile ^{13}CN **N** $= 2-1$.

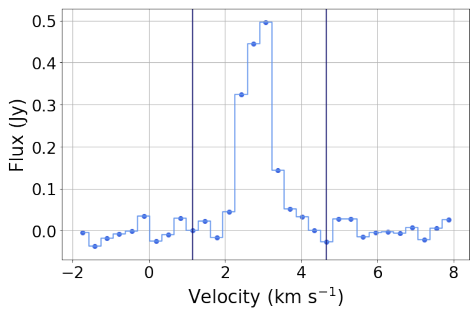

(c) Spectral profile C^{18}O J $= 2-1$.

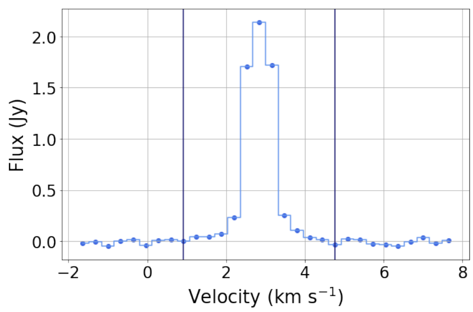

(d) Spectral profile ^{13}CO J $= 2-1$.

Fig. 4: An overview of all spectral line profiles. The vertical lines indicate the width used to create the moment 0 maps with.

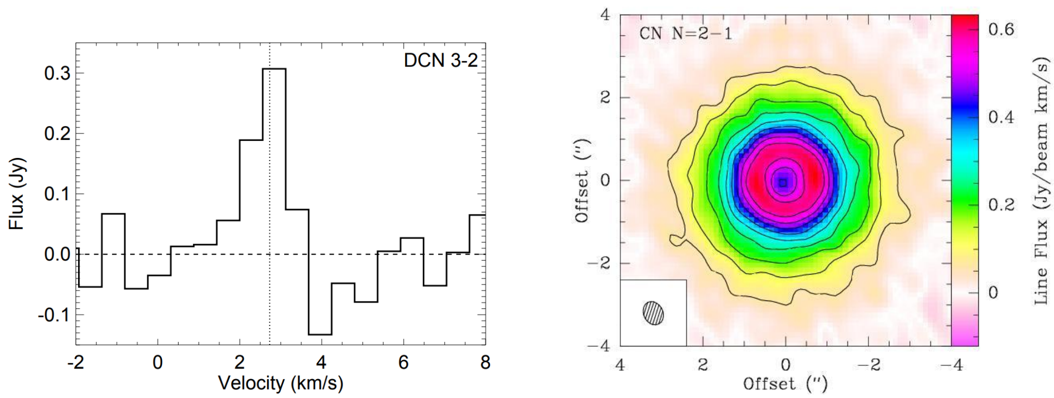

Fig. 5: Images used for flux comparison. Left: Spectral profile DCN J $= 3-2$, credit: [Qi et al., 2008]. Right: Moment 0 map CN **N** $= 2-1$, credit: [Teague et al., 2016].

4.4 Radial flux profiles

The radial flux profiles of the lines are shown in Fig. 6 and Fig. 7, where in the latter the continuum is plotted as well. Plotting them together allows for the comparison of their shapes, as features in the line profile might be caused by the continuum. We can use half the beam size as an indication of the error in the radius. This is roughly 15 AU and indicated by a blue bar in the figures. The radial flux profile of DCN $J = 3-2$, Fig. 6a, shows a lack of flux in the inner regions of the disk. The peak flux is reached at a distance of around 42 ± 15 AU and after that the flux goes down gradually. For ^{13}CN $\mathbf{N} = 2-1$ the radial flux profile, Fig. 6b, reaches a local minimum at approximately 18 ± 15 AU and it peaks at around 42 ± 15 AU . The reliability of this profile is doubtful however, as the data is very noisy, see the moment maps in Fig. 3c and Fig. 3d. For both C^{18}O $J = 2-1$ and ^{13}CO $J = 2-1$ the maximum flux is attained in the centre of the disk. It goes down steadily at first, then flattens between approximately (30-65) ± 15 AU. After that the flux decreases until it reaches the minimum flux at the edge of the disk. For the C^{18}O $J = 2-1$ and ^{13}CO $J = 2-1$ line we can see that their particular shape is not the same as the continuum. This is an indication that the plateau visible is a property of the gas emission.

From both the moment map and the radial profile the size of the hole in the DCN $J = 3-2$ emission can be determined. First the moment map. Measuring the darker-blue inner region gives a size of 0.35 to 0.4 arcsec. Converting this to AU, using the distance to the disk, gives a diameter of 21-24 AU or a radius of 10.5-12 AU. As no to very little emission is coming from this region it can be seen as a lower limit on the radius. The previous size determination is made purely by eye. From the radial flux profile, an upper limit can be defined quantitatively by looking at the location of the peak flux. Note that this is a true upper limit and probably does not represent the size of the hole well. This is mainly because the annulus of emission extends quite far. Looking at the peak flux thus overestimates the size of the hole, as can be seen in the moment maps (Fig. 3a and 3b). The peak flux occurs at a radius of approximately 42 ± 15 AU. The radius of the hole is thus between 10.5 and 42 AU.

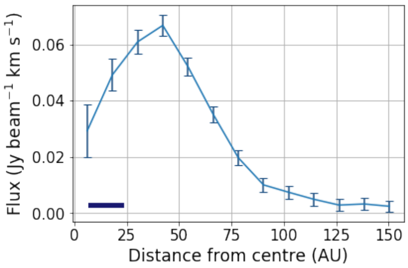

(a) Radial flux profile DCN J = 3 − 2.

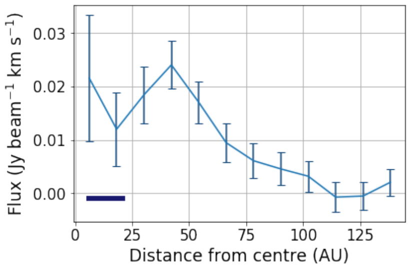

(b) Radial flux profile ^{13}CN **N** = 2 − 1.

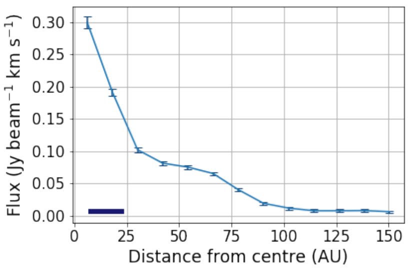

(c) Radial flux profile C^{18}O J = 2 − 1.

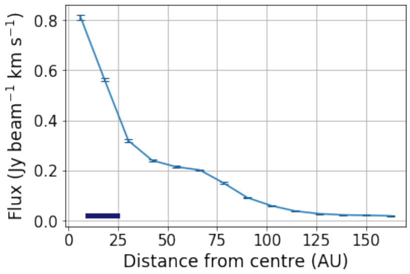

(d) Radial flux profile ^{13}CO J = 2 − 1.

Fig. 6: Overview of all radial flux profiles. The bar in the lower left indicates half of the beam size. Errors were made by dividing the rms noise in the moment 0 maps by the square root of the number of independent beams in each annulus.

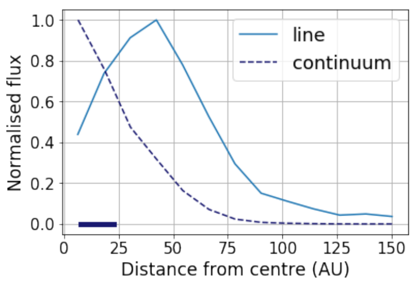

(a) Radial flux profile DCN J = 3 − 2 with continuum.

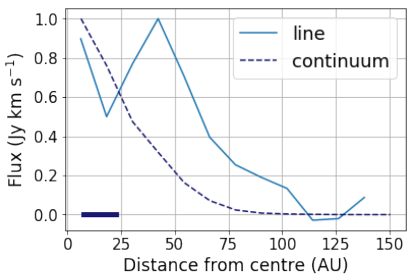

(b) Radial flux profile ^{13}CN **N** = 2 − 1 with continuum.

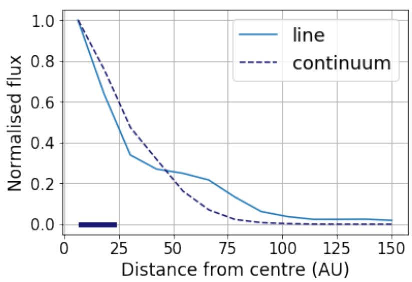

(c) Radial flux profile C^{18}O J = 2 − 1 with continuum.

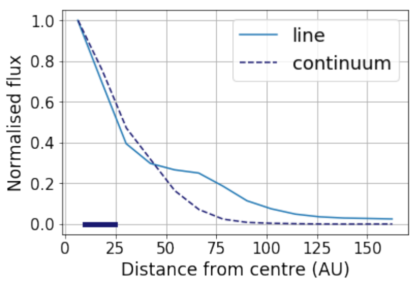

(d) Radial flux profile ^{13}CO J = 2 − 1 with continuum.

Fig. 7: Overview of all radial flux profiles with continuum, both normalised to 1. The bar in the lower left indicates half of the beam size.

4.5 $C^{18}O$ and ^{13}CO

4.5.1 Comparison of the $C^{18}O$ and ^{13}CO radial flux profiles to the literature

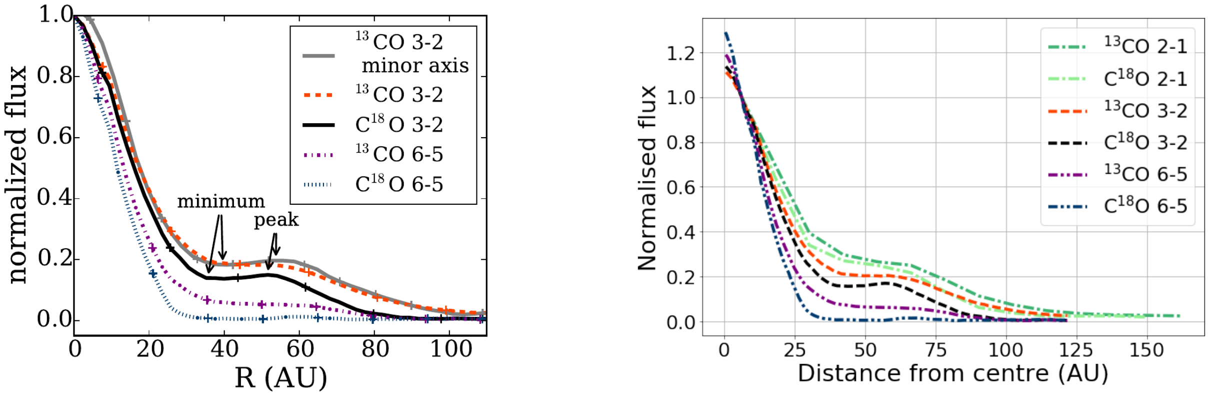

Fig. 8: Normalised radial flux profiles of CO isotopologues. Left: Profile from the literature, crosses are points with half beam separation, credit: [Schwarz et al., 2016]. Right: Comparison of own results to [Schwarz et al., 2016].

The particular shapes of the $C^{18}O$ $J = 2 - 1$ and ^{13}CO $J = 2 - 1$ radial flux profiles have been observed previously for other transitions of the same molecule, as can be seen in Fig. 8 [Schwarz et al., 2016]. A plot comparing my radial flux profile to those of Schwarz can be seen in Fig. 8b. My lines fit in well with Schwarz's. As can be seen in their data, higher transitions (6-5) go down steeper than lower ones (3-2), and for a certain transition the ^{13}CO lies above the $C^{18}O$. This trend is followed by my lines, they are a 2-1 transition and lie on top of all the other lines, with the ^{13}CO $J = 2 - 1$ above the $C^{18}O$ $J = 2 - 1$. The stacked pattern of the lines, all lying above or below each other, is due to the different transitions becoming optically thick at different depths in the disk. Each transition probes into a different layer (and thus temperature) of the disk, causing the pattern.

4.5.2 Temperature profiles for $C^{18}O$ and ^{13}CO

As described in Sect. 3.6 optical depths and radial temperature profiles were derived following the procedure of Schwarz. The radial optical depth profile can be seen in Fig. 9. It shows that the assumption of the ^{13}CO $J = 2 - 1$ being optically thick holds, as the optical depth is larger than 1 for most of the disk. Beyond a distance of approximately 90 AU it gets very close to one, the assumption may thus fail here. When comparing my results with [Schwarz et al., 2016], a clear difference is visible. First of all, my values seem to generally be on the low side with a temperature of 16 K on the plateau compared to 21 K for Schwarz. Another difference is that my temperature stays higher at 100 AU, 9 K compared to 0K for Schwarz. The qualitative shapes agree reasonably, but the absolute values not.

4.6 CO^+

The moment 0 maps of the CO^+ in spectral window four and five are shown in Fig. 11. They show only noise. For CO^+ $J = 2-1$, $\mathbf{F} = \frac{3}{2} - \frac{1}{2}$ the rms is 0.0032 Jy beam^{-1} km s^{-1}, corresponding to a flux of 0.046 Jy km s^{-1}. For CO^+ $J = 2 - 1$, $\mathbf{F} = \frac{5}{2} - \frac{3}{2}$ the rms is 0.0029 Jy beam^{-1} km s^{-1}, corresponding to a flux of 0.040 Jy km s^{-1}.

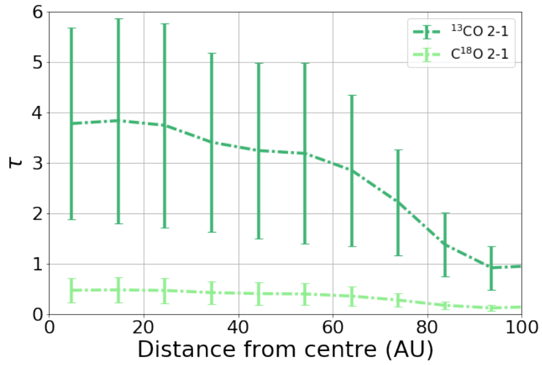

Fig. 9: Radial optical depth profile for the optical depths of $C^{18}O$ J = 2 − 1 and ^{13}CO J = 2 − 1. Errors shown were made by introducing a 1σ error in τ.

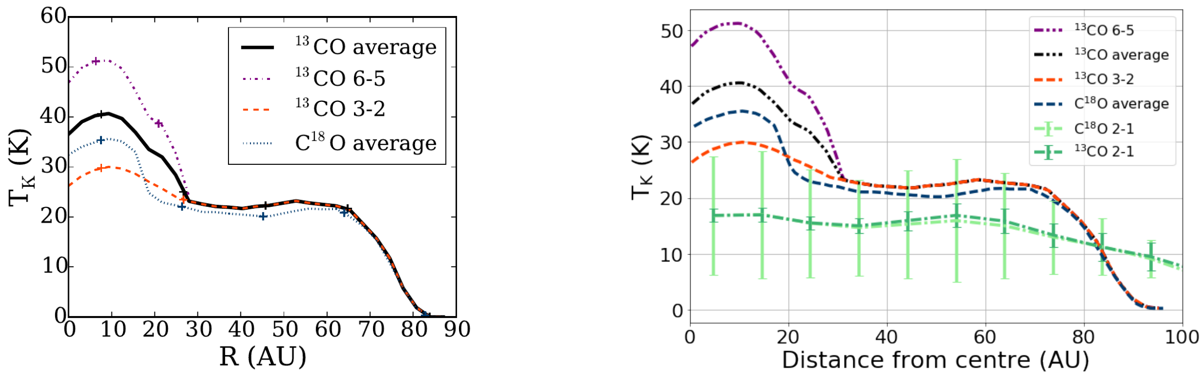

Fig. 10: Radial temperature profiles of the CO isotopologues. Left: Profile from the literature. Crosses are points with half beam separation, credit: [Schwarz et al., 2016]). Right: Comparison of own results to [Schwarz et al., 2016]. Errors were made by introducing a 1σ error in τ used to calculate T_K.

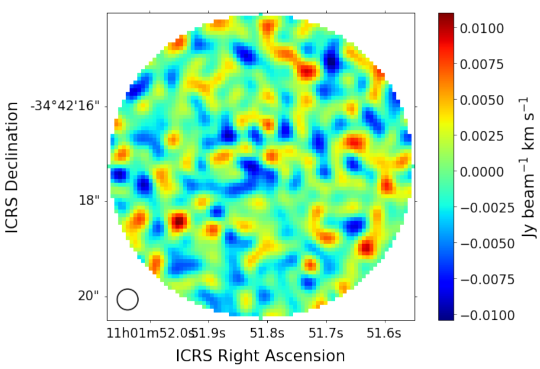

(a) Moment 0 map, CO^+ J = 2 − 1, $\mathbf{F} = \frac{3}{2} - \frac{1}{2}$.

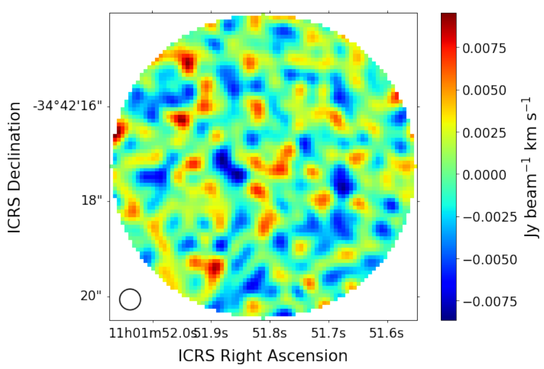

(b) Moment 0 map, CO^+ J = 2 − 1, $\mathbf{F} = \frac{5}{2} - \frac{3}{2}$.

Fig. 11: The moment 0 maps for CO^+.

5 Discussion

5.1 DCN

As seen in both the moment 0 map of DCN J $= 3-2$ (Fig. 3a) and its radial flux profile (Fig. 6), a hole is visible in its centre. This can have two reasons. First it is possible that there really is a hole, a region in which no DCN emission is present. The second option is that there is a process which causes a false impression of a hole. A previous observation of DCN J $= 3-2$ in TW Hya showed a centrally peaked distribution [Öberg et al., 2012]. In this previous observation the disk was barely resolved, with a beamsize of 2.8 $\times$ 2.3 arcsec [Öberg et al., 2012]. The beamsize of the data used in this thesis is 0.488 $\times$ 0.475 arcsec. Any structure present in the disk has been smeared out in the previous observation.

The over-subtraction of continuum emission may cause the false impression of a hole, as the process of subtracting the continuum may cause the removal of line emission [Weaver et al., 2018]. For DCN J $= 3-2$ the flux is quite low flux as noted in Table 3. Besides that, the radial flux profile (Fig. 7a) shows that the flux of DCN J $= 3-2$ in the inner region goes down when the continuum emission goes up. As over-subtracting the continuum has a larger effect when the line emission itself is weaker, it may create a lack of line emission, or in other words a hole, for the DCN J $= 3-2$ line.

The continuum can also cause the hole in another way. Continuum emission is the strongest in the centre of the disk and may even become optically thick there. Now if the DCN J $= 3-2$ is emitted from depths closer to the midplane than the depth at which the continuum becomes optically thick, our vision is obscured by the continuum. This then creates a hole as the line emission cannot escape the disk to be observed.

The hole can also be caused by an absence of DCN, a real chemical hole. One reason for the existence of the hole could be the formation of DCN, as it can form via multiple, temperature dependent, paths. The first one starts out with the following reaction [Henning and Semenov, 2013], [Roueff et al., 2007]:

$$\mathrm{H_3^+ + HD \leftrightarrows H_2D^+ + H_2 + 232K.} \tag{8}$$

The deuterium in $\mathrm{H_2D^+}$ is then further converted into other deuterium bearing molecules, such as DCN, via various ion-molecule reactions [Henning and Semenov, 2013]. An example of such a reaction is [Huang et al., 2017]:

$$\begin{gathered}\mathrm{H_2D^+ + CO \rightarrow H_2 + DCO^+,}\\ \mathrm{DCO^+ + HNC \rightarrow DCNH^+ + CO,}\\ \mathrm{DCNH^+ + e^- \rightarrow DCN + H.}\end{gathered} \tag{9}$$

Other possible paths are [Henning and Semenov, 2013], [Roueff et al., 2007]:

$$\begin{gathered}\mathrm{CH_3^+ + HD \leftrightarrows CH_2D^+ + H_2 + 390K,}\\ \mathrm{C_2H_2^+ + HD \leftrightarrows C_2HD^+ + H_2 + 550K.}\end{gathered} \tag{10}$$

The reaction products, $\mathrm{CH_2D^+}$ and $\mathrm{C_2HD^+}$ can then undergo different reactions. To form DCN the following route using the more abundant $\mathrm{CH_2D^+}$ is taken [Roueff et al., 2007]:

$$\begin{gathered}\mathrm{N + CH_2D^+ \rightarrow DCN^+ + H_2,}\\ \mathrm{DCN^+ + H_2 \rightarrow DCNH^+ + H,}\\ \mathrm{DCNH^+ + e^- \rightarrow DCN + H.}\end{gathered} \tag{11}$$

The main formation paths of DCN thus start from H_2D^+, using the reactions in Eq.(8) and Eq.(9), or from CH_2D^+, using the reactions in Eq.(10) and Eq.(11). The temperatures shown in Eq.(8) and Eq.(10) indicate that the back reactions are endothermic, they require energy. For Eq.(8) the back reaction will thus also occur at lower temperatures than for Eq.(10). When the back reactions occur they destroy the reaction products needed to get to DCN. This means that the reactions can only produce DCN effectively in regions where the temperature is low enough for the back reaction not to be effective. Relating this to the disk's temperature, DCN can be formed via the reaction starting from Eq.(8) when temperatures are below 30 K, or via the reaction starting from Eq.(10) when temperatures are below 80 K [Öberg et al., 2012], [Henning and Semenov, 2013].

The radius at which temperatures drop below 30 K in the disk for DCN $J = 3-2$ will be determined in two ways. First it will be done using radial temperature profiles of CO isotopologues [Schwarz et al., 2016]. This profile (Fig. 10a) shows that in the inner region of the disk temperatures are higher than 30 K and then drop below it quite quickly. The $C^{18}O$ average line drops below 30 K at a radius of approximately 17 AU, or ~19 AU after the correction for the distance to TW Hya. Assuming DCN $J = 3-2$ traces a part of the disk slightly deeper than $C^{18}O$ does, it will trace a part of the disk that is slightly cooler, since gas temperatures in the disk drop as one gets closer to the midplane. This means that for DCN $J = 3-2$ temperatures drop below 30 K beyond a radius similar to or slightly smaller than 19 AU. Another way of determining this radius is using the icelines mentioned in the paper. The CO iceline is the radius in the disk where temperatures drop below the freeze-out temperature of CO, 21 K [Schwarz et al., 2016]. At the surface, this is at approximately 30 AU, while in the midplane it is calculated to be between 17-23 AU or ~19-26 AU after the correction for the distance. Temperatures of 30 K would thus be reached at distances closer to the star, at radii smaller than the ones just mentioned. Assuming DCN $J = 3-2$ traces quite deep in the disk, it will have temperatures $\gtrsim$ 30K at radii $\lesssim$ 19-26AU. From these two derivations based on [Schwarz et al., 2016], temperatures for DCN $J = 3-2$ drop below 30 K in the disk at radii $\gtrsim$ 19-26AU. From a chemical model for the gas temperatures in TW Hya it is confirmed that at these radii temperatures of 30 K are realistic [Kamp et al., 2013]. The hole in DCN $J = 3-2$ has a radius in between 10.5 and 42 AU. Assuming this upper limit overestimates the size of the hole, as explained in Sect. 4.4, the real radius lies closer to this lower limit.

To more clearly explain how chemistry may cause the hole, the discussion will be shortly summarised. For DCN $J = 3-2$ a hole is observed with a radius between 10.5 and 42 AU. The temperature for DCN $J = 3-2$ drops below 30 K at radii $\gtrsim$ 19-26AU. And finally there are two main pathways that form DCN. The reaction starting from Eq.(8) is effective at temperatures < 30 K, while the reaction starting from Eq.(10) can produce DCN effectively up to temperatures of 80 K. The radius of the hole matches with the radius for which temperatures drop below 30 K. An explanation for the hole could thus be that the formation pathway which produces DCN at temperatures up to 80 K (Eq.(10)) is not effective in the TW Hya disk. This means that DCN is mostly formed in regions colder than 30 K, and emission will thus only originate from these regions. As no DCN is formed closer to the star there will be no emission from this region, causing the hole.

DCN was also observed in several other protoplanetary disks, [Huang et al., 2017], with some of the disks also showing ring like structures. As argued in the paper this indicates quite complex chemistry for DCN which might be sensitive to the different stellar and disk properties of the observed targets. A more detailed study (e.g. chemical modelling) is required to fully understand the chemistry of DCN and the origin of the rings. This is out of the scope of this research project.

5.2 ^{13}CN

In the TW Hya disk, the detection of ^{13}CN is a first detection. The signal to noise ratio of this observation is low, 2. The flux ratio of ^{12}CN $\mathbf{N} = 2-1/^{13}$CN $\mathbf{N} = 2-1$ is found to be around 50, which is lower than the ^{12}C/^{13}C canonical ratio of 69 [Visser et al., 2018]. This can be explained by the fact that different chemical processes in the disk, such as photodissociation, may be isotope selective, deviating the ratio from the canonical value. The paper shows in that for a model of a protoplanetary disk (illuminated by a T Tauri star) column density ratios of ^{12}CN/^{13}CN are below this value of 69 and may reach 50 [Visser et al., 2018]. This is consistent with our observations.

In the disk there appears to be a certain structure for ^{13}CN $\mathbf{N} = 2-1$. The ring previously detected for ^{12}CN $\mathbf{N} = 2-1$ coincides well with the location of the peak fluxes present in the ^{13}CN $\mathbf{N} = 2-1$ moment 8 map. This indicates that there is a possibility that ^{13}CN $\mathbf{N} = 2-1$ has a similar ring-like structure as recorded for ^{12}CN $\mathbf{N} = 2-1$ [Cazzoletti et al., 2018]. According to the the chemical model we expect the isotopologues to be radially co-spatial, implying the rings would be at a similar position [Visser et al., 2018].

5.3 C^{18}O and ^{13}CO

The radial temperature profiles show that higher J transitions have higher temperatures, see Fig. 10. One reason for this is that the higher J transitions become optically thick at higher altitudes in the disk [Schwarz et al., 2016], [Fedele et al., 2016]. As the molecules trace the part of the disk in which they become optically thick, this means that the higher transitions trace closer to the surface, which is the warmer part of the disk. Besides that, higher J transitions are also excited at higher temperatures and emit here preferentially.

The temperature profile (10) was based on our moment 8 map (Fig. 3f and 3h). These show a certain structure, for ^{13}CO J $= 2-1$ there is a cross shaped region in which the flux is lower. This is most likely a consequence of our observational setup. The structure may be caused by the velocity resolution of our data. As the disk is not perfectly face on, the emission peaks at different observing frequencies in different parts of the disk. Emission from the part of the disk that is moving towards us will be slightly blue shifted (with respect to the systemic velocity) and will thus have a higher observing frequency. The part of the disk moving away from us will be slightly red shifted and thus have a lower observing frequency. This also shows when looking at the line cube. The emission starts in one part of the disk and moves through it in the different channels. The spacing between the channels is 0.32 km/s. This might be too large, as the emission jumps to the different parts of the disk when going through the channels of the line cube. In other words, the emission present in one channel is not followed smoothly by the emission in the next channel, some might be lost in the noise. Channels of the line cube displaying this phenomenon are shown in Fig. 12. Comparing the line cube with the moment 8 map of ^{13}CO, it showed that the lower flux cross in the moment 8 map coincides with this skipping of emission. In Schwarz's paper the reported velocity resolution is 0.1 km/s, roughly three times better than ours.

The structure present in the moment 8 map directly influences the values found for the kinetic gas temperature. This can be seen in the equations shown in Sect. 3.6. As some emission is skipped in our moment 8 map, the azimuthally averaged flux is lower than it should be. From Eq.(4) it can be seen that this directly influences the brightness temperature, making it smaller than it should be. To check that this is a possible explanation for the kinetic temperatures being consistently too low, it was decided to multiply the brightness temperatures by a factor accounting for this. By eye it was estimated that the impact on the azimuthally averaged flux is ~ 10 to 15 %. Therefore the kinetic temperature was recalculated with brightness temperatures multiplied by a factor 1.1 and 1.15 to see what the effects on the kinetic temperature would be (Fig. 13). Increasing the brightness temperature by these factors does not linearly increase the kinetic temperature. Therefore the increase in temperature of the first data point will be given. A factor 1.1 or 1.15 increase in the brightness temperature increases the kinetic temperature of the first data point by 3 and 5 K respectively. The 15 % increase affects the temperature enough such that the profile matches the literature. The lower velocity resolution is therefore a possible explanation for the temperature discrepancy between my work and Schwarz's work.

It has to be noted that in Schwarz's work no errors are given for the radial temperature profiles. Comparing the data quality of Schwarz with the data in this thesis does not show a significant difference in the signal to noise ratio. It can thus be assumed that if they had propagated the errors into the temperature profiles these would be significant.

The reason for wanting to derive these temperatures so accurately is that the flatness of the profiles between 20 and 70 AU indicates that the surface snowline of CO is traced. The plateau in the data shows that temperature stays constant over a large distance. This can be interpreted in the following way. Assuming no emission is coming from the ice, the CO can only trace down to the layer just above the ice. The temperature at which the profile flattens is thus the freeze out temperature of CO. In Schwarz's paper the profile flattens at 21 K which is consistent with the expected freeze out temperature of CO binding to a primarily CO ice surface [Schwarz et al., 2016]. If the temperature of this plateau is lower, as seen in my data (Fig. 10b), this indicates that there might be gas present in the ice reservoir. This can occur when photodesorption, the process in which a photon causes the desorption of a molecule from the dust, takes place.

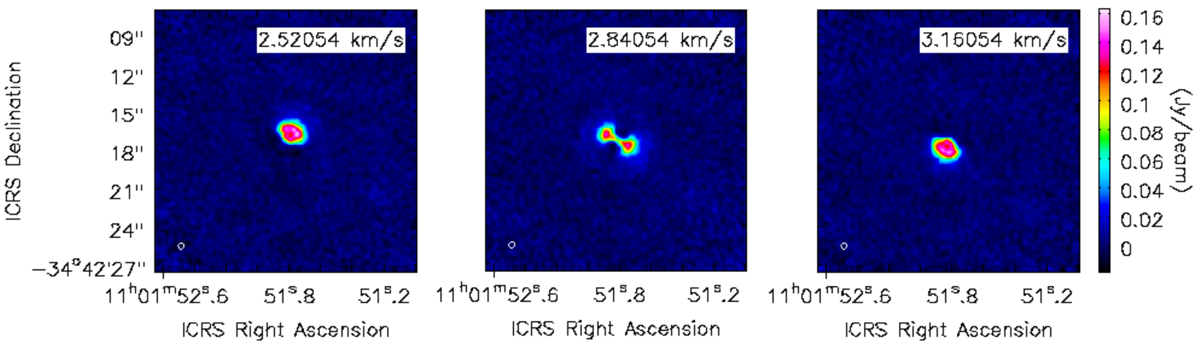

Fig. 12: 3 channels from the ^{13}CO line cube, the corresponding velocities are shown in the upper right corner. The images show how the emission jumps to different parts of the disk.

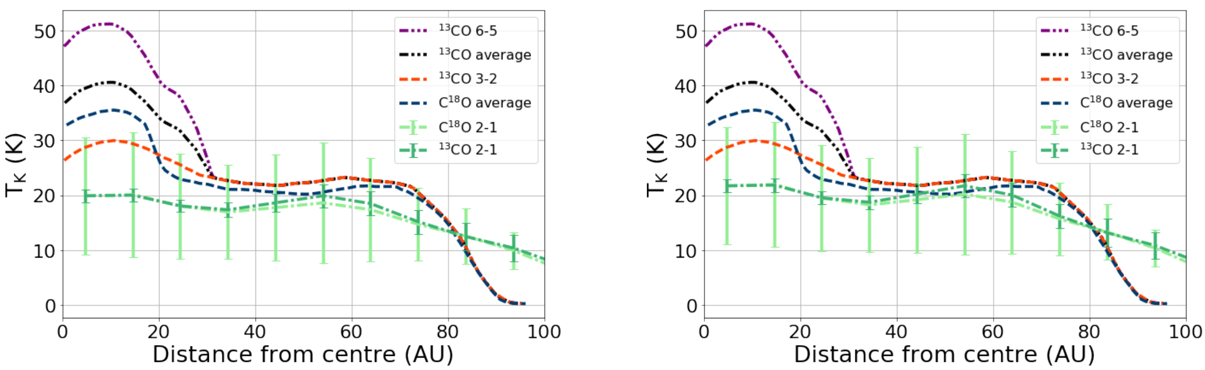

Fig. 13: Radial temperature profiles, our T_K recalculated with T_B modified, comparison of own results to [Schwarz et al., 2016]. Left: T_B multiplied by a factor 1.1. Right: T_B multiplied by a factor 1.15.

6 Conclusion and future ideas

In this thesis, ALMA data of the protoplanetary disk TW Hya was analysed. In the data set, four lines were found, namely: DCN J = 3 − 2, ^{13}CN **N** = 2 − 1, C^{18}O J = 2 − 1 and ^{13}CO J = 2 − 1. The line fluxes found for the lines are: 0.331 ± 0.093 Jy km s^{-1} for DCN J = 3 − 2, 0.10 ± 0.16 Jy km s^{-1} for ^{13}CN **N** = 2 − 1, 0.63 ± 0.22 Jy km s^{-1} for C^{18}O J = 2 − 1 and 2.28 ± 0.30 Jy km s^{-1} for ^{13}CO J = 2 − 1. These all match the literature within 3σ, except for ^{13}CN **N** = 2 − 1, as this is a first detection. It was compared to the flux of the more common ^{12}CN **N** = 2 − 1 and the flux was found to be approximately 50 times lower, roughly comparable with chemical models [Visser et al., 2018].

Moment maps and radial flux profiles were made to show the structure of the line emission. The DCN J = 3 − 2 emission appears ring shaped with no emission coming from the centre. The hole in the inner region has a radius between 10.5 and 42 AU. The presence of this hole can be explained in several ways. It could just be false impression of a hole caused by the over-subtraction or optical thickness of the continuum. It can also be caused by the chemical formation pathway. If DCN is not formed in the hotter parts of the disk, no emission will be observed here, causing a hole. The ^{13}CN **N** = 2−1 has a too low signal to noise ratio to determine a definite shape, though it does not seem to be centrally peaked. The moment 8 map shows that the peak fluxes coincide well with the ring found for ^{12}CN **N** = 2 − 1 [Cazzoletti et al., 2018], indicating that ^{13}CN **N** = 2 − 1 may have a similar ring structure.

The emission from C^{18}O J = 2 − 1 and ^{13}CO J = 2 − 1 are both centrally peaked. The radial flux profiles show a plateau in the emission, where the profile flattens between (30-65) ± 15 AU. This is in line with the literature, which has similar profiles for the J = 6 − 5 and J = 3 − 2 transitions. For C^{18}O J = 2 − 1 and ^{13}CO J = 2 − 1 radial temperature profiles were made as well. They show a flat profile with temperatures around 16 K in the inner 60 AU, which then gradually decrease to ∼ 8 K at 100 AU. Compared to literature these temperatures seem to be consistently on the lower side, though this may be explained by the velocity resolution of our data. The shapes of these profiles appears to match with the literature.

Lastly, upper limits were determined for the fluxes of non-detected lines. These are 0.046 Jy km s^{-1} for the CO^{+} J = 2 − 1, **F** = $\frac{3}{2} - \frac{1}{2}$ transition and 0.040 Jy km s^{-1} for the CO^{+} J = 2 − 1, **F** = $\frac{5}{2} - \frac{3}{2}$ transition.

In the future, observations with higher spatial resolution cold be taken for the DCN J = 3 − 2 and ^{13}CN **N** = 2 − 1 line, as both show an interesting structure in the disk. To draw definite conclusions for ^{13}CN **N** = 2 − 1, the sensitivity of the data should also be improved. This can be done by observing for a longer period of time, though some improvement can also be made by re-reducing the dataset instead of using the pipeline product directly. If the rings are really present, further research could be done to determine which processes cause these structures.

To learn more about the temperature structure of the disk other transitions of C^{18}O and ^{13}CO more transitions could be investigated. Each transition traces a different depth, and thus temperature, in the disk. By looking at more transitions a more detailed temperature profile of this face on disk can thus be made.

Finally the cause for the difference between the radial temperature profiles made in this thesis and those by Schwarz could be investigated further. To be able to properly compare the results the process of creating the radial temperature profiles should be the same for both data sets. To do this their data would need to be re-binned to account for the difference in spectral resolution. After that either the method used in Schwarz's paper or the method used in this thesis should be used for both data sets.

References

[ALMA (ESO/NAOJ/NRAO), 2019] ALMA (ESO/NAOJ/NRAO) (2019). Alma. https://www.almaobservatory.org/en/home/. (Accessed on 06/06/2019).

[Andrews et al., 2016] Andrews, S. M., Wilner, D. J., Zhu, Z., Birnstiel, T., Carpenter, J. M., Pérez, L. M., Bai, X.-N., Öberg, K. I., Hughes, A. M., and Isella, A. (2016). Ringed Substructure and a Gap at 1 au in the Nearest Protoplanetary Disk. *ApJ*, 820(2):L40.

[Appenzeller and Mundt, 1989] Appenzeller, I. and Mundt, R. (1989). T Tauri stars. *A&AR*, 1(3-4):291–334.

[Brown and Carrington, 2003] Brown, J. M. and Carrington, A. (2003). *Rotational Spectroscopy of Diatomic Molecules*. Cambridge Molecular Science. Cambridge University Press.

[Cazzoletti et al., 2018] Cazzoletti, P., van Dishoeck, E. F., Visser, R., Facchini, S., and Bruderer, S. (2018). CN rings in full protoplanetary disks around young stars as probes of disk structure. *A&A*, 609:A93.

[de Pater and Lissauer, 2015] de Pater, I. and Lissauer, J. (2015). *Planetary Sciences*. Cambridge University Press.

[Drążkowska and Alibert, 2017] Drążkowska, J. and Alibert, Y. (2017). Planetesimal formation starts at the snow line. *A&A*, 608:A92.

[Ercolano and Pascucci, 2017] Ercolano, B. and Pascucci, I. (2017). The dispersal of planet-forming discs: theory confronts observations. *Royal Society Open Science*, 4:170114.

[Favre et al., 2013] Favre, C., Cleeves, L. I., Bergin, E. A., Qi, C., and Blake, G. A. (2013). A Significantly Low CO Abundance toward the TW Hya Protoplanetary Disk: A Path to Active Carbon Chemistry? *ApJ*, 776(2):L38.

[Fedele et al., 2016] Fedele, D., van Dishoeck, E. F., Kama, M., Bruderer, S., and Hogerheijde, M. R. (2016). Probing the 2D temperature structure of protoplanetary disks with Herschel observations of high-J CO lines. *A&A*, 591:A95.

[Gaia Collaboration, 2018] Gaia Collaboration (2018). VizieR Online Data Catalog: Gaia DR2 (Gaia Collaboration, 2018). *VizieR Online Data Catalog*, page I/345.

[Henning and Semenov, 2013] Henning, T. and Semenov, D. (2013). Chemistry in Protoplanetary Disks. *Chemical Reviews*, 113(12):9016–9042.

[Huang et al., 2018] Huang, J., Andrews, S. M., Cleeves, L. I., Öberg, K. I., Wilner, D. J., Bai, X., Birnstiel, T., Carpenter, J., Hughes, A. M., Isella, A., Pérez, L. M., Ricci, L., and Zhu, Z. (2018). CO and Dust Properties in the TW Hya Disk from High-resolution ALMA Observations. *ApJ*, 852(2):122.

[Huang et al., 2017] Huang, J., Öberg, K. I., Qi, C., Aikawa, Y., Andrews, S. M., Furuya, K., Guzmán, V. V., Loomis, R. A., van Dishoeck, E. F., and Wilner, D. J. (2017). An ALMA Survey of $DCN/H^{13}CN$ and $DCO^+/H^{13}CO^+$ in Protoplanetary Disks. *ApJ*, 835(2):231.

[Isella et al., 2016] Isella, A., Guidi, G., Testi, L., Liu, S., Li, H., Li, S., Weaver, E., Boehler, Y., Carperter, J. M., and De Gregorio-Monsalvo, I. (2016). Ringed Structures of the HD 163296 Protoplanetary Disk Revealed by ALMA. *Physical Review Letters*, 117(25):251101.

[Kamp et al., 2013] Kamp, I., Thi, W. F., Meeus, G., Woitke, P., Pinte, C., Meijerink, R., Spaans, M., Pascucci, I., Aresu, G., and Dent, W. R. F. (2013). Uncertainties in water chemistry in disks: An application to TW Hydrae. *A&A*, 559:A24.

[McMullin et al., 2007] McMullin, J. P., Waters, B., Schiebel, D., Young, W., and Golap, K. (2007). CASA Architecture and Applications. In Shaw, R. A., Hill, F., and Bell, D. J., editors, *Astronomical Data Analysis Software and Systems XVI*, volume 376 of *Astronomical Society of the Pacific Conference Series*, page 127.

[NRAO, 2012] NRAO (2012). Splatalogue. http://www.cv.nrao.edu/php/splat/. (Accessed on 06/25/2019).

[Öberg et al., 2012] Öberg, K. I., Qi, C., Wilner, D. J., and Hogerheijde, M. R. (2012). Evidence for Multiple Pathways to Deuterium Enhancements in Protoplanetary Disks. *ApJ*, 749(2):162.

[Qi et al., 2004] Qi, C., Ho, P. T. P., Wilner, D. J., Takakuwa, S., Hirano, N., Ohashi, N., Bourke, T. L., Zhang, Q., Blake, G. A., and Hogerheijde, M. (2004). Imaging the Disk around TW Hydrae with the Submillimeter Array. *ApJL*, 616(1):L11–L14.

[Qi et al., 2008] Qi, C., Wilner, D. J., Aikawa, Y., Blake, G. A., and Hogerheijde, M. R. (2008). Resolving the Chemistry in the Disk of TW Hydrae. I. Deuterated Species. *ApJ*, 681(2):1396–1407.

[Rohatgi, 2019] Rohatgi, A. (2019). Webplotdigitizer. https://automeris.io/WebPlotDigitizer/. (Accessed on 06/04/2019).

[Roueff et al., 2007] Roueff, E., Parise, B., and Herbst, E. (2007). Deuterium fractionation in warm dense interstellar clumps. *A&A*, 464(1):245–252.

[Salinas et al., 2017] Salinas, V. N., Hogerheijde, M. R., Mathews, G. S., Öberg, K. I., Qi, C., Williams, J. P., and Wilner, D. J. (2017). DCO^+, DCN, and N_2D^+ reveal three different deuteration regimes in the disk around the Herbig Ae star HD 163296. *A&A*, 606:A125.

[Savage et al., 2002] Savage, C., Apponi, A. J., Ziurys, L. M., and Wyckoff, S. (2002). Galactic $^{12}C/^{13}C$ Ratios from Millimeter-Wave Observations of Interstellar CN. *ApJ*, 578(1):211–223.

[Schwarz et al., 2016] Schwarz, K. R., Bergin, E. A., Cleeves, L. I., Blake, G. A., Zhang, K., Öberg, K. I., van Dishoeck, E. F., and Qi, C. (2016). THE RADIAL DISTRIBUTION OF H2 AND CO IN TW HYA AS REVEALED BY RESOLVED ALMA OBSERVATIONS OF CO ISOTOPOLOGUES. *The Astrophysical Journal*, 823(2):91.

[Teague et al., 2016] Teague, R., Guilloteau, S., Semenov, D., Henning, T., Dutrey, A., Piétu, V., Birnstiel, T., Chapillon, E., Hollenbach, D., and Gorti, U. (2016). Measuring turbulence in TW Hydrae with ALMA: methods and limitations. *A&A*, 592:A49.

[Visser et al., 2018] Visser, R., Bruderer, S., Cazzoletti, P., Facchini, S., Heays, A. N., and van Dishoeck, E. F. (2018). Nitrogen isotope fractionation in protoplanetary disks. *A&A*, 615:A75.

[Weaver et al., 2018] Weaver, E., Isella, A., and Boehler, Y. (2018). Empirical Temperature Measurement in Protoplanetary Disks. *ApJ*, 853(2):113.

[Woitke et al., 2009] Woitke, P., Kamp, I., and Thi, W. F. (2009). Radiation thermo-chemical models of protoplanetary disks. I. Hydrostatic disk structure and inner rim. *A&A*, 501(1):383–406.